Model Parameter and Performance Calculation of Cylindrical Wound-Rotor Synchronous Motors

M. Mabhula, *Student Member, IEEE*, and M. J. Kamper, *Senior Member, IEEE*

***Abstract*—The paper details modern saturation modeling and performance calculation to the analysis of grid-connected cylindrical wound-rotor synchronous motors. The developed models give reliable results with limited computation effort. The finite element based method uses iterative procedures to calculate the motor performance during which the motor parameters are evaluated in detail. Experimental results prove that the method has a high degree of accuracy and is computationally efficient.**

***Index Terms*—Finite element method, frozen permeabilities method, synchronous motors, modeling, open and short circuit, wound-rotor.**

I. Introduction

THE striving for positive economic growth rates in the world causes energy demand (specifically electric energy) to increase and also so the negative footprint of higher energy consumption. In order to make this increased energy demand and energy consumption sustainable, there is strong pressure on the acquisition of clean energy, the storage of energy and the effective consumption of energy. In large numbers of energy processes, at some point in the process, the energy is converted from mechanical energy to electrical energy or vice versa. Hydro- and wind-energy systems are examples where mechanical energy is converted into electrical energy. Regarding energy storage e.g. we have the well-known gravity water pump storage systems where there is a continuous conversion from mechanical energy to electrical energy and vice versa. Also in the consumption of electrical energy, 60–70% of all generated electrical energy in the world is converted to mechanical energy. A huge amount of this energy conversion is required to drive large pumps, fans and compressors. Hence, the electromechanical energy converter (that is the electrical machine) plays a tremendous role in all energy engineering. If the energy efficiencies of electric machines can be improved, a great deal of energy is saved [1]. The latter is particular important for wound-rotor synchronous machines as these machines are used in large energy conversion systems [2].

Manuscript received February 4, 2020; revised April 24, 2020; accepted June 29, 2020. Date of publication July 7, 2020; date of current version February 19, 2021. The authors would like to thank Stellenbosch University, Stellenbosch, South Africa for financial funding in support of this study. Paper no. TEC-00130-2020. *(Corresponding author: Mkhululi Mabhula.)*

The authors are with the Department of Electrical and Electronic Engineering, Stellenbosch University, Stellenbosch 7600, South Africa (e-mail: mabhulamkhululi@gmail.com; kamper@sun.ac.za).

Color versions of one or more of the figures in this article are available online at https://ieeexplore.ieee.org.

Digital Object Identifier 10.1109/TEC.2020.3007715

To increase the energy efficiency of the electric machine, accurate modeling and model parameter estimation are required for the optimum design and control of the electrical machine. Many of the electrical machine systems today utilize power electronic drive converters to obtain adjustable speed drive. If the optimum control of the machine is known or understood, the machine can be controlled very energy efficient at a specific operating point. For applications with fixed supply voltage and frequency connection, the electric machine must be optimally designed for highest energy efficiency for the specific load condition - it is known that many installed electrical machine systems run very inefficiently in industry.

However, non-linear magnetic materials are used in electrical machines that make the accurate modeling and model parameter calculation of the machine difficult. It has been shown that classical models do not give good power prediction of electric machines [2] and that non-classical methods must be used to accurately determine the electrical machine characteristics for accurate control [3]. If the modeling and model parameters of the electric machine are accurate, then (i) accurate performance estimation together with accurate design optimization can be done and (ii) the control of the electric machine can be done much more energy efficient.

Accurate modeling of the non-linear magnetic material property of the electric machine is thus a problem [4], [5]. In addition, there is the problem of determining accurately the parameters of the non-linear model. A further challenge is to determine the parameters computational efficient [6], [7]; with powerful computers, solving complex problems, computational efficient nowadays means more and more energy-efficient. A final issue is that there are so many different electrical machines in the industry today: not have only induction and synchronous machines anymore, but also permanent magnet, reluctance and flux switching electrical machines to name a few. The problem is that the models and parameters of these machines differ and it also differs whether the machine is small or big.

This paper presents a modern saturation modeling method of the traditional grid-connected three-phase large wound-rotor synchronous motor (WRSM) used in a wide range of industries for their unique application of high mechanical power demand, power system control and plant power factor correction. The accurate but fast method suited for design optimization gives a good grasp of mathematical formulation and operation of the WRSM by incorporating all major saturation effects (i.e. saturation saliency, asymmetric saturation and cross-axes magnetization) [3]–[5], [8], [9]. Further explanation and experimental

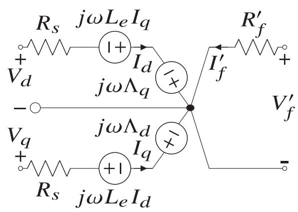

Fig. 1. Steady state dqf equivalent circuit diagram.

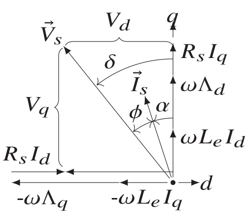

Fig. 2. Stator voltage and current space phasor diagram.

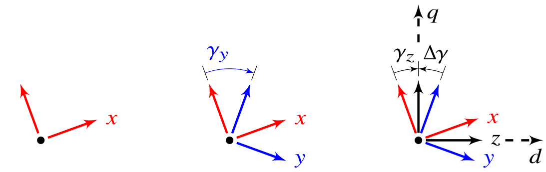

Fig. 3. Shifting motor magnetic field axis (d-axis) under load.

validation of the method is presented, with the goal to predict accurately and fast the steady-state performance of the WRSM. Additional discussions are given in explaining the measured performance results using the method-predicted motor parameters.

II. Modeling

The steady-state stator voltage phasor $\vec{V}_s$ components, including the end-winding inductance L_e effect, and the rotor voltage V_f of the motor, are respectively given by

$$\begin{cases} V_d &= R_s I_d - \omega L_e I_q - \omega \Lambda_q \\ V_q &= R_s I_q + \omega L_e I_d + \omega \Lambda_d, \end{cases} \tag{1}$$

and

$$V_f = R_f I_f, \tag{2}$$

where Λ_d, Λ_q are the d and q axes stator total flux linkages (excluding end leakage), R_s the stator resistance and I_d, I_q the stator dq-axes current components. The end-winding inductance calculation is given in [10]. In (2), R_f is the equivalent rotor field resistance and I_f the field current. From (1) and (2), the dqf-axes equivalent circuit of Fig. 1 and the phasor diagram of Fig. 2, result. In Fig. 1, the rotor parameters of (2) have been referred to the stator (denoted by $'$) using the effective winding ratio. From Fig. 2, the stator voltage and current phasors are respectively defined by

$$\vec{V}_s : \begin{cases} V_d = -V_s \sin(\delta) \\ V_q = V_s \cos(\delta) \end{cases} \text{ and } \vec{I}_s : \begin{cases} I_d = -I_s \sin(\alpha) \\ I_q = I_s \cos(\alpha), \end{cases} \tag{3}$$

where V_s, I_s are the stator voltage, current phasor magnitudes and δ, α the stator voltage, current phasor angles.

For economic use of lamination material, most industrial motors either operate near or in deep saturation. Hence, the phenomenon of saturation saliency, cross-axes magnetization and asymmetric saturation will always exist in these motors. To incorporate the latter in the motor model, three field magnetic axis positions are defined as x, y and z shown in Fig. 3. The x-axis is the classically defined magnetic field axis (aligned with the rotor field winding) in which the motor is analyzed on assumed perfect decoupled dq-axes. Modeling on the x-axis defines the total flux linkage components of (1) in terms of inductances as

$$x\text{-axis model} : \begin{cases} \Lambda_d = L_{dd} I_d + L_{df} I_f \\ \Lambda_q = L_{qq} I_q. \end{cases} \tag{4}$$

In (4), there are no mutual cross-axis inductances and for a round-rotor $L_{dd} = L_{qq}$.

Due to saturation, the x-axis is shifted by an angle γ_y (saliency shift angle) to the y-axis, shown in Fig. 3. On the y-axis, the impact of cross-axes magnetization is a well-known phenomenon, especially for sensorless control designers [3]. Incorporating cross-axes magnetization, (4) is redefined as

$$y\text{-axis model} : \begin{cases} \Lambda_d = L_{dd} I_d + M_{dq} I_q + L_{df} I_f \\ \Lambda_q = M_{qd} I_d + L_{qq} I_q. \end{cases} \tag{5}$$

Furthermore, due to the rotor field excitation that causes asymmetric saturation in the rotor, the magnetic field axis is shifted away from the shifted y-axis to the z-axis by an angle $\Delta\gamma$ as shown in Fig. 3. The angle $\Delta\gamma$ defines a further error in the magnetic field position. The z-axis is the true magnetic field axis of the motor. Modeling on the z-axis redefines (5) as

$$z\text{-axis model} : \begin{cases} \Lambda_d = L_{dd} I_d + M_{dq} I_q + L_{df} I_f \\ \Lambda_q = M_{qd} I_d + L_{qq} I_q + M_{qf} I_f. \end{cases} \tag{6}$$

In motor analysis, the saliency (γ_y) and field (γ_z) angles can also be used as a measure to the severity of the magnetic axis shift phenomenon, which shows the importance of incorporating saturation effects into the motor modeling.

The model of (6) is considered complete in the motor modeling of this paper. Thus according to (1), the motor terminal voltage can only be correctly computed by determining the self-inductances (L_{dd}, L_{qq}), the effect of the rotor current on the d-axis inductance (L_{df}) and the cross-axis inductances (M_{dq}, M_{qd}, M_{qf}), as expressed in (4)–(6).

Now using (6) in (1) and combining (1) and (2), the terminal voltage is expressed by

$$\begin{bmatrix} V_d \\ V_q \\ V_f \end{bmatrix} = \begin{bmatrix} (R_s - \omega M_{qd}) & -\omega(L_{qq} + L_e) & -\omega M_{qf} \\ \omega(L_{dd} + L_e) & (R_s + \omega M_{dq}) & \omega L_{df} \\ 0 & 0 & R_f \end{bmatrix} \begin{bmatrix} I_d \\ I_q \\ I_f \end{bmatrix}, \tag{7}$$

simplified to

$$[V] = [Z][I]. \tag{8}$$

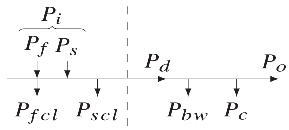

Fig. 4. Simplified power flow diagram.

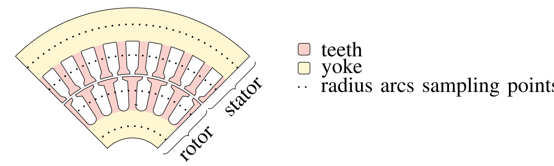

Fig. 5. Pole face axial view lamination flux density sampling points.

Also using (6), for a p-pole pair motor, the torque

$$T_e = 1.5p(\Lambda_d I_q - \Lambda_q I_d), \tag{9}$$

is defined as a sum of three inductance-function calculated torques given by

$$T_e = T_f + T_s + T_m, \tag{10}$$

where

$$\begin{cases} T_f = 1.5p(L_{df} I_q - M_{qf} I_d) I_f \\ T_s = 1.5p(L_{dd} - L_{qq}) I_d I_q \\ T_m = 1.5p(M_{dq} I_q^2 - M_{qd} I_d^2). \end{cases} \tag{11}$$

The power factor angle $\phi = \delta - \alpha$, shown in Fig. 2, is calculated from

$$\cos(\phi) = \sin(\delta)\sin(\alpha) + \cos(\delta)\cos(\alpha), \tag{12}$$

as

$$\phi = \cos^{-1}((V_d/V_s)(I_d/I_s) + (V_q/V_s)(I_q/I_s)). \tag{13}$$

The percentage efficiency of the motor is calculated from the simplified power flow diagram of Fig. 4 as

$$\eta = (P_o/P_i) \times 100\%, \tag{14}$$

where P_i and P_o are the electrical input and mechanical output powers respectively. In (14), the electrical input power is the sum of the stator and the rotor electrical input powers, as

$$P_i = P_s + P_f = P_o + P_l. \tag{15}$$

In (15), P_l is the total loss expressed as

$$P_l = P_{scl} + P_{fcl} + P_{bw} + P_c, \tag{16}$$

where P_{scl} is the stator copper loss, P_{fcl} the rotor copper loss, P_{bw} the bearing and windage losses and P_c the core loss. The stator and rotor copper losses are calculated from

$$P_{scl} = 1.5 I_s^2 R_s, \qquad P_{fcl} = I_f^2 R_f. \tag{17}$$

The mechanical losses, which comprises of bearing and windage losses i.e. $P_{bw} = P_b + P_w$, are respectively given as [11]

$$P_b = 0.5\omega\mu_f F d_b, \qquad P_w = k_\rho D_r (l + 0.6\tau_p) v_r^2, \tag{18}$$

where F, μ_f, v_r, τ_p and d_b are the bearing load, friction coefficient, surface speed, pole pitch length and the inner diameter of the shaft bearing respectively. For the 2D lamination of the motor shown in Fig. 5, the core losses of (16) are estimated by

$$P_c = m f^n (B_t^o M_t + B_y^o M_y), \tag{19}$$

where B_t and B_y are the maximum teeth and yoke flux densities, M_t and M_y are the teeth and yoke mass, and the constants m, n, o are according to [12] for the considered lamination material. The maximum flux density values are obtained from the FEM flux densities on arc sample points indicated in Fig. 5. The mechanical power output of (14) is calculated from

$$P_o = P_d - (P_{bw} + P_c), \tag{20}$$

where P_d is the mechanical developed power expressed from (9) as

$$P_d = \omega T_d. \tag{21}$$

III. Problem 1: Machine Inductance Calculation

Considering the complete model of Section II, given the motor excitation currents I_d, I_q and I_f, the net total flux linkages of (6), calculated from the non-linear static FEM solution, must be decomposed to calculate the self and mutual inductance parameters. Because it is impossible to implement the conventional non-linear FEM analysis to decompose these flux linkages, a FEM based method of freezing the motor core permeabilities is employed to separate these flux linkages into corresponding contributions of different excitations. In the method, the mesh element magnetic permeabilities obtained from the non-linear FEM solution at an operating point load of the motor, are frozen to preserve all the information about saturation in the motor. Henceforth, the solution problem becomes linear, in which three linear FEM solutions due to I_d, I_q and or I_f are necessary to decompose (6). The above discussed total flux linkage decomposition using the frozen permeability method is described in the following steps [4]:

1) A non-linear FEM solution at the desired operating point at an arbitrary rotor position is conducted. From this solution, the total dq-axes flux linkages (excluding end leakages) are calculated, defined by

$$\text{non-linear}: \begin{cases} \Lambda_d = \Lambda_d(I_d, I_q, I_f) \\ \Lambda_q = \Lambda_q(I_d, I_q, I_f), \end{cases} \tag{22}$$

which in turn can be used to calculate the electromagnetic torque of (9). Also from the non-linear FEM solution the actual torque of the motor can be calculated using the magnetic stress tensor.

2) The FEM permeabilities of all the mesh elements of step 1) are saved and frozen. This enables saturation levels not to change with different excitations.

3) Using the frozen permeabilities and the same FEM model of steps 1) and 2), the decomposed dq-axes flux linkages

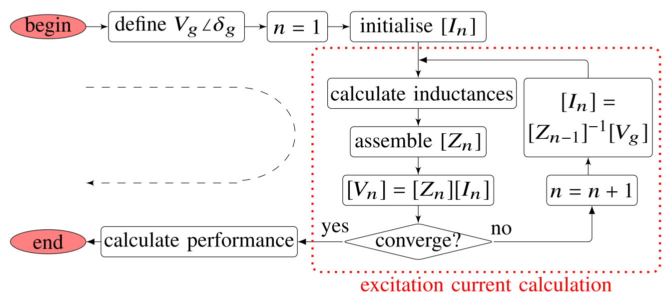

Fig. 6. Iterative procedure flow diagram for excitation current calculation.

of (6), solved using single excitations, are defined as

$$1^{\text{st}}\text{linear}: \begin{cases} \Lambda_{dd}(I_d) = L_{dd}I_d = \Lambda_d(I_d, 0, 0) \\ \Lambda_{qd}(I_d) = M_{qd}I_d = \Lambda_q(I_d, 0, 0), \end{cases} \tag{23}$$

$$2^{\text{nd}}\text{linear}: \begin{cases} \Lambda_{dq}(I_q) = M_{dq}I_q = \Lambda_d(0, I_q, 0) \\ \Lambda_{qq}(I_q) = L_{qq}I_q = \Lambda_q(0, I_q, 0), \end{cases} \tag{24}$$

$$3^{\text{rd}}\text{linear}: \begin{cases} \Lambda_{df}(I_f) = L_{df}I_f = \Lambda_d(0, 0, I_f) \\ \Lambda_{qf}(I_f) = M_{qf}I_f = \Lambda_q(, 0, 0, I_f). \end{cases} \tag{25}$$

Consequently, the inductance parameters are calculated by means of the three linear FEM solutions of (23)–(25) as

$$1^{\text{st}}\begin{cases} L_{dd} = \Lambda_{dd}/I_d \\ M_{qd} = \Lambda_{qd}/I_d \end{cases} 2^{\text{nd}}\begin{cases} M_{dq} = \Lambda_{dq}/I_q \\ L_{qq} = \Lambda_{qq}/I_q \end{cases} 3^{\text{rd}}\begin{cases} L_{df} = \Lambda_{df}/I_f \\ M_{qf} = \Lambda_{qf}/I_f. \end{cases} \tag{26}$$

From (26) and with R_s, R_f known, $[Z]$ of (8) according to (7) is assembled.

IV. Problem 2: Current Calculation

The important feature of the FEM used in Section III is that in its basic form requires a defined current $[I]$, whereas in actual grid-connected motor applications relates to a defined stator voltage $[V]$ and load. For that, an iterative procedure, shown in Fig. 6 is proposed for determining the excitation currents for a given grid voltage magnitude V_g and load angle δ_g according to (3).

Following Fig. 6, the arbitrary initial current $[I_n]$ ($n = 1$) is used to calculated the initial inductances as to assemble the initial $[Z_n]$. With the initial $[I_n]$ and $[Z_n]$, the corresponding initial $[V_n]$ of (8) is computed, which might not be equal to the grid defined terminal voltage $[V_g] = [-V_g \sin(\delta_g) V_g \cos(\delta_g) V_f]^T$. If not equal a next iteration ($n + 1$) is executed as shown in Fig. 6. For this, a new current is calculated, shown in Fig. 6 as

$$[I_n] = [Z_{n-1}]^{-1}[V_g]. \tag{27}$$

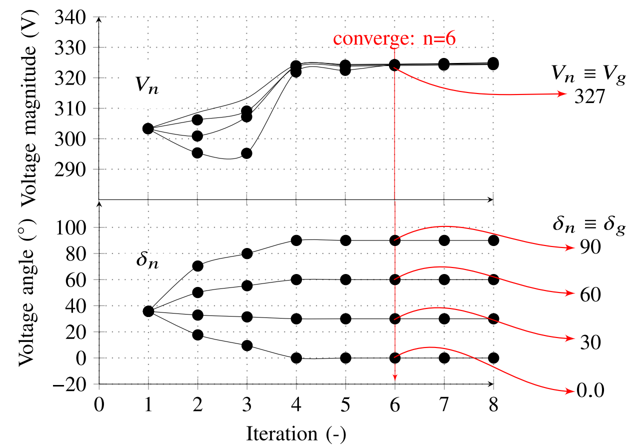

Fig. 7. Calculated stator voltage magnitude and angle variation during the iterative procedure with constant grid voltage magnitude and field current.

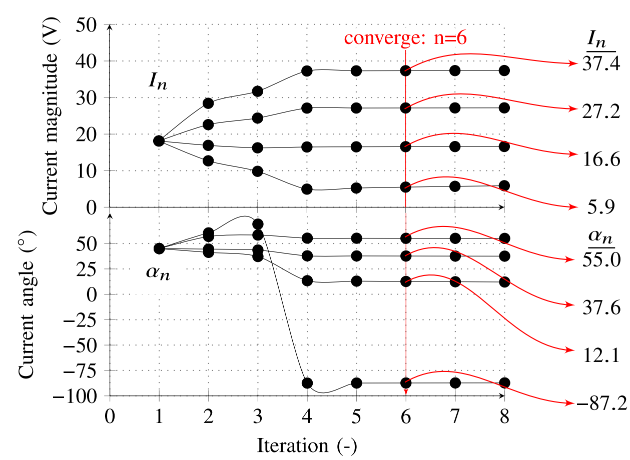

Fig. 8. Calculated stator current magnitude and angle variation during the iterative procedure with constant grid voltage magnitude and field current.

The procedure is repeated for each cycle until convergence, that is when

$$|V_n - V_g| \leqslant 0.5\nu(V_n + V_g), \tag{28}$$

where ν is the fraction tolerance in the voltage value. At this point, it can be confirmed that the calculated current is the correct FEM excitation current according to the defined grid voltage and load. It must be noted from Fig. 6 that each iteration consists of $1\times$ slow non-linear plus $3\times$ very-fast linear static FEM solutions.

Fig. 7 shows the variation of V_n and δ_n on a selected WRSM (10 kW, 400 V, 4-pole, 50 Hz) with field current $I_f = 23$ A to attain a defined grid voltage $V_g = 327$ V of angles δ_g equal to 0, 30, 60 and 90°. Fig. 8 shows the corresponding calculated I_n and α_n. Using $\nu = 0.001$ in (28), the iterative process is shown terminates at the 6$^{\text{th}}$ iteration ($n = 6$), but it is clear that at $n = 4$ very accurate results are already obtained. On a 3.6 GHz CPU with 16 GB RAM Intel(R) Core(TM) i7 computer, the 6 iterations take about 9 s for the considered mesh of the motor. This is far better in computational time when compared to other

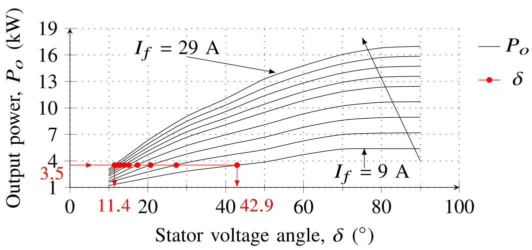

(a) Power output map with field current a parameter and supply voltage a constant

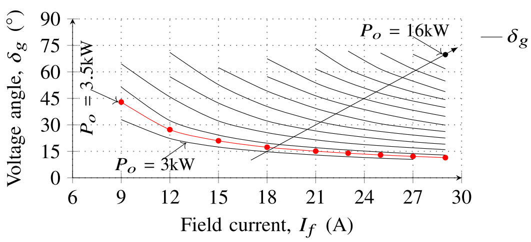

(b) Voltage angle map with power output a parameter

Fig. 9. Calculated perfomance maps of the motor at a 400 V, 50 Hz supply for (a) power output and (b) grid voltage angle.

FEMs such as time-harmonic and time-stepping [13], [14]. It is important to state from Figs. 7 and 8 that the motor parameters δ_n, I_n and α_n can also be used to test for convergence, though with a slight modification of Fig. 7 in the case of I_n and α_n.

One element for convergence analysis is the initialization of the current. In order to help for a faster convergence, it is typically recommended to initialize using the grid-voltage estimated current, by using an estimated (typical) impedance matrix. However, arbitrary current initialization works well for convergence as demonstrated in Figs. 7 and 8. Nevertheless, Figs. 7 and 8 provably show that convergence is even independent of the unknown motor defined load angle i.e. δ_g, a problem dwelt with in Section V.

V. Problem 3: Grid Load Angle Calculation

In actual grid-connected motor applications the grid load angle δ_g given in the iterative process of Fig. 6 is unknown. To predict this load angle according to the load of the motor, the use of performance maps are proposed. To speed up time, these maps are constructed by parallelizing the iterative process of Fig. 6 in which each parallel task is given a different load angle δ_g. The parallelizing is done by using python's multiprocessing modules. The performance maps of the motor are constructed against the load angle for different field currents. An example of this for the motor under study is shown in Fig. 9(a) where P_o of (20) is plotted as a function of δ_g for field currents $9 \leqslant I_f \leqslant 29$ A.

From the map of Fig. 9(a) for given P_os, the δ_g map of Fig. 9(b) is generated using python splines. A case is shown for $P_o = 3.5$ kW in Fig. 9(a) which is mapped to δ_g as shown in Fig. 9(b). With the δ_g map of Fig. 9(b) available of the motor understudy, the designer can quickly determine the load angle δ_g for a given machine output power and field current.

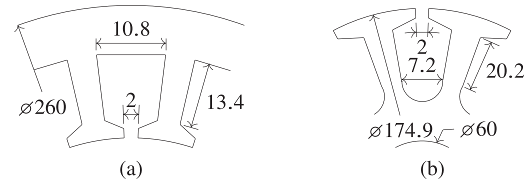

Fig. 10. Prototyped motor (a) stator and (b) rotor dimensions (mm).

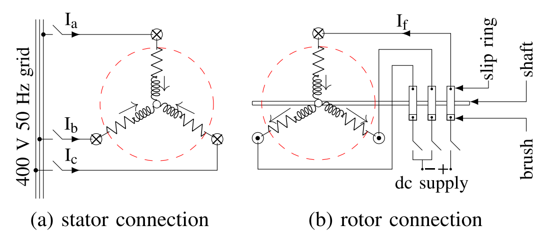

Fig. 11. Winding excitation connection for (a) stator and (b) rotor.

TABLE I
Motor Specifications

Variable	Stator	Rotor	Variable	Stator	Rotor
resistance (Ω)	0.5	1.2	turns per slot	16	32
slots	36	24	pole pairs p	2	2
air gap (mm)	0.31		stack length (mm)	125	

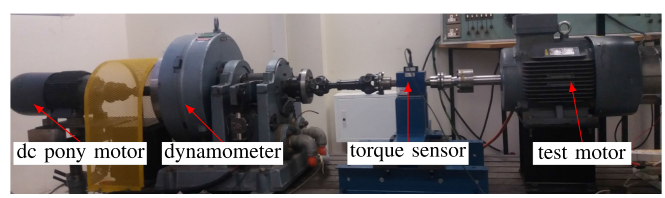

Fig. 12. Experimental laboratory test bench setup.

It must be emphasized again that the performance maps of Fig. 9 can be quickly generated by parallelizing tasks. This shows the effectiveness of the iterative process in the calculation of the grid load angle δ_g for an actual grid-connected motor application.

VI. Measured and Predicted Open and Short Circuit Curves

The lamination dimensions, winding connection and specifications of the test motor are shown respectively in Figs. 10, 11 and given in Table I. The test bench system is shown in Fig. 12. The dynamometer in Fig. 12 is mechanically coupled to the test motor through the torque sensor to provide the mechanical load. The torque sensor is used to measure the speed and power output P_o. The dc pony motor in Fig. 12 is used for synchronization and the open and short circuit tests of the motor.

The measured open and short circuit curves are obtained by operating the motor at constant synchronous speed and measuring the stator open circuit voltage and short circuit current as a

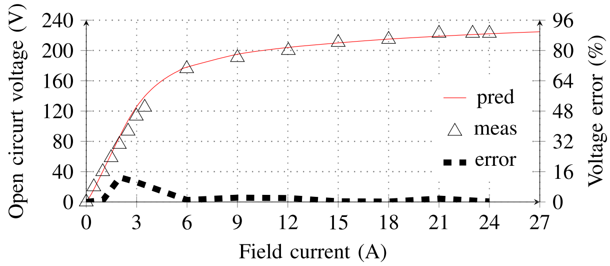

Fig. 13. Measured (meas), predicted (pred) and percentage error (error) of open circuit voltage versus field current at synchronous speed.

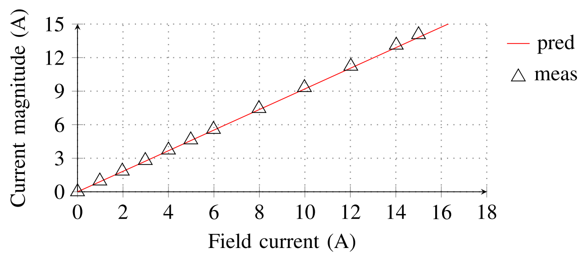

Fig. 14. Measured (meas) and predicted (pred) stator short circuit current versus field current at synchronous speed.

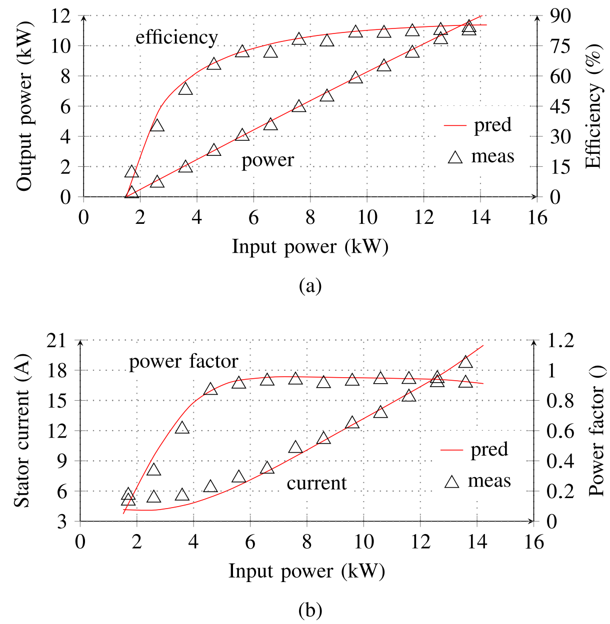

Fig. 15. Measured (meas) and predicted (pred) performance curves versus electrical input power with constant field current.

function of field current respectively. These measured results of the prototyped test motor are shown in Figs. 13 and 14.

The open circuit curve of the prototyped test motor is predicted from (8) as

$$[V_{oc}] = [Z_{oc}][I_{oc}] \quad \text{where} \quad I_s = 0, \tag{29}$$

by using $1\times$ FEM non-linear solution for each field current. The predicted open circuit curve is shown in Fig. 13. This is shown to be in good agreement with the measured results as revealed by the stator open circuit voltage percentage error (calculated by utilizing cubic spline interpolate curves) in Fig. 13, with a maximum percentage error of 12% at 2 A field current.

For the predicted short circuit curve of the prototyped test motor, the proposed iterative procedure in Section IV is used. For this V_g in Fig. 6 is set to $V_g = 0$ for each field current. The predicted short circuit curve is shown in Fig. 14. Excellent agreement is shown in Fig. 14 between measured and predicted results, which confirms the powerfulness of the proposed iterative procedure.

VII. Measured and Predicted Load Performance

For the measured load performance, the prototyped test motor is synchronized with the 400 V grid supply and loaded by varying the dynamometer power in the test bench of Fig. 12. For these tests, the field current was set constant $I_f = 23$ A and the winding temperature monitored at 75°C. The measured load performance results as a function of input power are shown in Fig. 15.

To predict the load performance, the iterative process of Fig. 6 is used in which the grid load angle is calculated using the mapping technique given in Section V. The performance curves of power factor, efficiency, power input, power output and current are predicted by (12), (14), (15), (20) and (27) respectively. The predicted load performance curves as a function of input power are shown in Fig. 15. This shows good agreement between predicted and measured load performance. The slight difference in the power factor and current in Fig. 15(b) at low input powers can be explained by the FEM used BH curve. This aspect is further considered in Sub-section VIII-A.

VIII. Predicted Parameter Curves

In addition the previous section itemized problem solutions, the other advantage of the proposed iterative procedure is the continuous access to accurately calculated motor parameters for better motor analysis and understanding. This is demonstrated in this section for the test conditions of the motor in Sections VI and VII.

A. Open and Short Circuit Parameter Curves

From the measured open circuit voltage V_{rms} and field current I_f of Fig. 13, the measured stator open circuit field inductance is calculated as

$$L_{df} = V_q/(\omega I_f) = \sqrt{2}V_{\text{rms}}/\omega I_f. \tag{30}$$

The corresponding predicted L_{df}, using (29) is calculated from the non-linear FEM solution as

$$L_{df} = \Lambda_{df}/I_f \tag{31}$$

Note that M_{qf} is not considered with only I_f excitation as it is found to be always zero as expected.

Fig. 16 shows a good agreement between the measured and predicted parameters of (30) and (31) respectively. Also shown in Fig. 16 is the FEM used M400-50A lamination BH curve, which explains the behavior of the predicted L_{df} of (31) at low

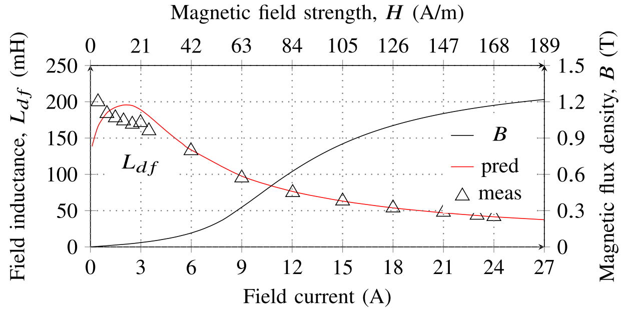

Fig. 16. Measured (meas) and predicted (pred) stator open circuit field inductance and manufacturer's M400-50A BH curve.

H (and low I_f) values. The latter also explains the mentioned slight difference between the measured and predicted load performance curves of Fig. 15(b) at low input powers. Fig. 16 illustrates the expected phenomenon of saturation in the motor which decreases the L_{df} as the field current increases.

For the short circuit curve analysis, Fig. 17(a) shows the predicted current components of the predicted short circuit current of Fig. 14. Note from Fig. 17(a) that $I_q \approx 0$ as expected. Furthermore, the short circuit flux linkages due tot I_d, I_q and I_f of Fig. 17(a) are shown in Fig. 17(b) and(c). The corresponding inductances calculated from (23)–(26) using Fig. 17(a) and (c) are shown in Fig. 17(d). As expected, both the short circuit mutual flux linkages $M_{dq}I_q = M_{qd}I_d = M_{qf}I_f \approx 0$ and inductances $M_{dq} = M_{qd} = M_{qf} \approx 0$ since $I_q \approx 0$, henceforth, not shown in Fig. 17(c) and (d). However, what is illuminating from the results of Fig. 17(d) is the increase in the short circuit inductances (up to 19%) with field current, which is classically assumed constant in literature. Thus, the latter assumption is incorrect in the considered motor, and saturation saliency should always be taken into account due to the increase of the main flux $\Lambda_s = \sqrt{\Lambda_d^2 + \Lambda_q^2}$ as shown in Fig. 17(b).

B. Load Performance Parameter Curves

Fig. 18 shows the corresponding calculated motor parameters using the proposed iterative process following the results of Fig. 15. Fig. 18(a) and (b) show the solved current components and current angle. It can be seen from the positive d-axis current at a lower input power of Fig. 18(a) that the motor is under excited.

Fig. 18(c)–(e) show other motor parameters in which the effect of saturation is noticed. It is evident that cross-axes magnetization, saturation saliency and asymmetric saturation have a significant effect on the parameters of the test motor. As the motor is loaded, the d-axis comes out of saturation as shown by the decrease in the d-axis flux linkages of Fig. 18(c). Consequently, the d-axis L_{dd} and field L_{df} inductances increase with an increase in the d-axis negative current shown in Fig. 18(d) due to less saturation in the corresponding magnetic axis. At lower q-axis current, the d-axis inductance is not significantly affected by cross-magnetization i.e. $M_{dq} \approx 0$. However, as the q-axis current increase, the effect of cross magnetization is noticed. The above described d-axis inductance analysis can be

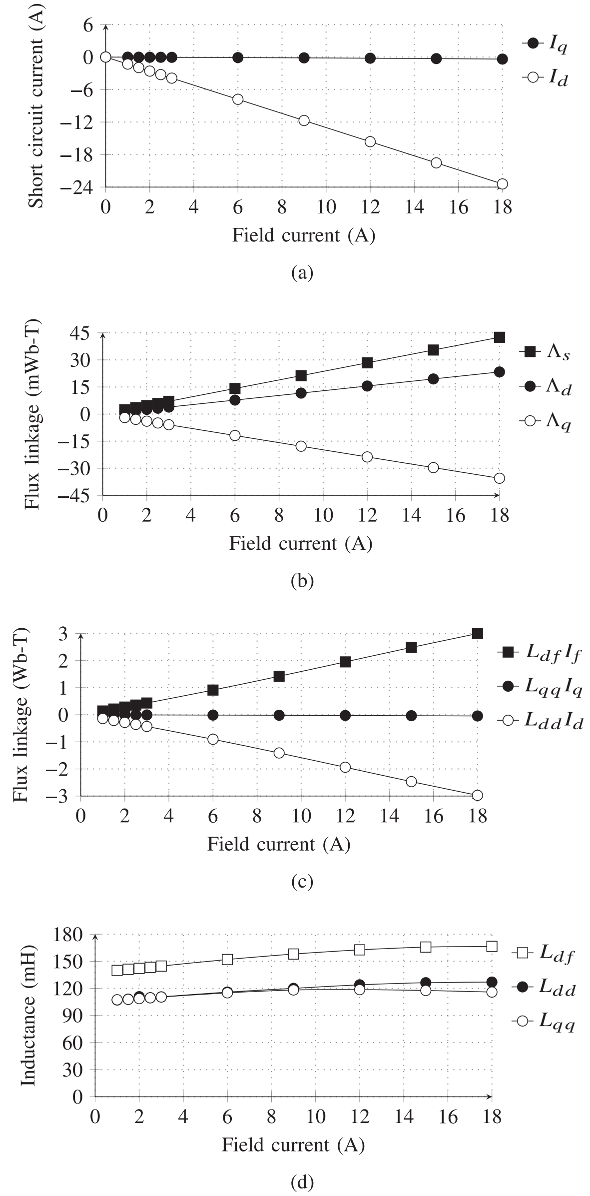

Fig. 17. Calculated stator short circuit (a) current phasor components, (b), (c) flux linkages, and (d) inductance versus field current at synchronous speed.

repeated for the q-axis inductances, in which it was found that for the considered motor $M_{dq} = M_{qd}$. The effect of saturation saliency is noticed in Fig. 18(d) where for a cylindrical rotor motor $L_{dd} \neq L_{qq}$ as the motor is subjected to load. The effect of asymmetric saturation is also noticed in Fig. 18(d) which introduces the negative q-axis mutual field inductance M_{qf} larger than the cross-axes inductances M_{dq}, M_{qd} as the motor is loaded.

Fig. 18(e) shows the different torque components which are directly calculated from the current and inductances of Fig. 18(a) and (d) using (11). In Fig. 18(e), T_a is the average of the FEM calculated torque. The effect of cross-axes magnetization and saturation saliency brings in negative and positive mutual T_m and saliency T_s torques, which drastically reduces the resultant torque T_d from the field torque T_f at higher input powers.

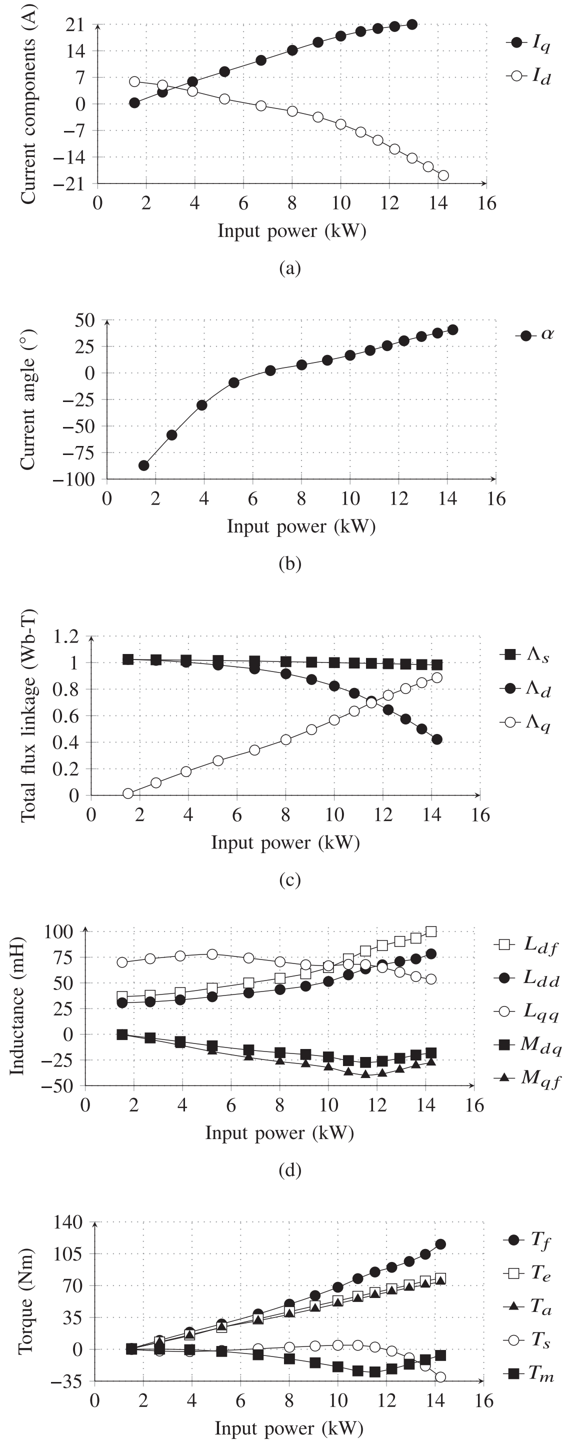

Fig. 18. Calculated stator (a) current components, (b) current angle, (c) flux linkages, (d) inductances, and (e) torques at a constant field current.

IX. Application

It is important to highlight that the calculated power performance map of Fig. 9(b) also comes with corresponding motor parameter and performance information. Different from inverter-fed motors, the application of the power performance map of Fig. 9(b) is essential for grid-connected motors where the designer has only knowledge of the grid voltage magnitude, the load power and the field current. Using the power performance map all the motor parameter and performance information such as the impedance matrix, current and efficiency of the motor is available for different loads. So the latter is different from current-controlled inverter-fed motors where the current vector is the known input, and from which the motor performance can be calculated using dq-axes inductance-current maps.

The fastness and compatibility of the proposed performance calculation method as demonstrated in the previous sections makes the method extremely suited for the design optimization of the WRSM. This is demonstrated in [12] where the NSGA-II optimization algorithm is utilized for a Pareto-front formation of optimal WRSM designs.

An important part of the modeling of electrical motors under fault conditions is to determine the motor's fault model parameters [15]. As the developed model parameter calculation method in the paper gives accurately the complete model parameters of the healthy motor, it can be used in the parameter estimation for condition monitoring of the WRSM.

Although the study in the paper is done on a small WRSM, the parameter and performance calculation method is also applicable for large power level applications. This is because the additional loss components of eddy and proximity effects in the stator copper layers of large motors can analytically be accounted for as in [16], which perfectly fits with the proposed calculation method. An example of a large power application is the use of the proposed method to accurately predict the rotor field current necessary of a WRSM synchronous condenser to adjust the required reactive power or to improve the power factor of the load system.

X. Conclusion

In this paper calculation methods based on FE static solutions are developed for accurate calculation of the complete parameter model and performance of WRSMs. From the study, the following conclusions are drawn: 1) The complete motor model of the WRSM that includes the effects of saliency, cross-magnetization and asymmetric saturation is shown can be determined for given stator and rotor currents by means of only one rotor position, one non-linear and three linear static FE solutions. The accuracy of the calculation is confirmed by measurements. 2) The proposed iterative procedure for determining the stator and rotor currents of the grid-connected (voltage-fed) WRSM is shown converge under all loading conditions of the WRSM within four to six iterations. 3) The proposed method for determining the load performance map of the WRSM that is necessary to calculate the grid load angle of the motor is shown to be very effective in determining accurately and fast the short circuit and load parameters and load performance of the WRSM. This is proved to be a useful tool in analyzing the measured open/short-circuit and load test results in terms of parameter change, torque components and magnetic axis shift. 4) The existence of a third (true) magnetic field axis is defined and confirmed by inductance calculation in the paper in which loading the WRSM has a non-linear effect on the shift of this axis.

ACKNOWLEDGMENT

The authors would like to thank Stellenbosch University for financial funding in support of this study. The authors wish to acknowledge Kenan Cloete and the staff of the Electrical Workshop of the Stellenbosch University for the assistance in the laboratory experimental tests.

REFERENCES

[1] M. M. S. Dezfouli, M. Z. A. Yazid, A. Zakaria, S. F. Ahmed, A. Ali, and S. Moghimi, "Application of high efficiency motors in HVAC system for energy saving purpose," in *Proc. IEEE Int. Conf. Innovative Res. Develop.*, May 2018, pp. 1–5, doi: 10.1109/ICIRD.2018.8376309.

[2] T. Wisniewski, J. Vannier, B. Lorcet, J. Saint-Michel, and X. Jannot, "Extended dq modeling of wound-rotor synchronous machines with dampers for transient analysis," in *Proc. 18th Int. Symp. Electromagn. Fields Mechatronics, Elect. Electron. Eng. Book Abstr.*, Sep. 2017, pp. 1–2, doi: 10.1109/ISEF.2017.8090768.

[3] N. Bianchi, E. Fornasiero, and S. Bolognani, "Effect of stator and rotor saturation on sensorless rotor position detection," *IEEE Trans. Ind. Appl.*, vol. 49, no. 3, pp. 1333–1342, May 2013.

[4] M. Mabhula and M. J. Kamper, "Saliency and mutual inductance effect in cylindrical wound-rotor synchronous motor," in *Proc. IEEE Workshop Elect. Mach. Des., Control Diagnosis*, Apr. 2017, pp. 152–157.

[5] J. Pang, W. Liu, N. Jiao, J. Wang, and P. Ma, "Calculation of cross-coupling inductance and electromagnetic torque in wound-rotor synchronous starter/generator," *IEEE Trans. Ind. Electron.*, vol. 66, no. 7, pp. 5115–5123, Jul. 2019.

[6] S. Mezani, T. Hamiti, L. Belguerras, T. Lubin, and C. Gerada, "Computation of wound rotor induction machines based on coupled finite elements and circuit equation under a first space harmonic approximation," *IEEE Trans. Magn.*, vol. 52, no. 3, pp. 1–4, Mar. 2016.

[7] M. Mabhula and M. J. Kamper, "Computational efficient parameter and performance prediction of wound-rotor induction motor," *IEEE Trans. Magn.*, vol. 54, no. 6, pp. 1–7, Jun. 2018.

[8] B. Stumberger, G. Stumberger, D. Dolinar, A. Hamler, and M. Trlep, "Evaluation of saturation and cross-magnetization effects in interior permanent-magnet synchronous motor," *IEEE Trans. Ind. Appl.*, vol. 39, no. 5, pp. 1264–1271, Sep. 2003.

[9] S. T. Lee, T. A. Burress, and L. M. Tolbert, "Power-factor and torque calculation with consideration of cross saturation of the interior permanent magnet synchronous motor with brushless field excitation," in *Proc. IEEE Int. Electric Mach. Drives Conf.*, May 2009, pp. 317–322.

[10] M. J. Kamper, "The design criteria and development of a design program for squirrel-cage induction motors for use in the load region," Master's thesis, Dep. Elect. Electron. Eng., Stellenbosch University, Stellenbosch, South Africa, Dec. 1987.

[11] J. Pyrhoenen, T. Jokinen, and V. Hrabovcova, *Design of Rotating Electrical Machines*. Hoboken, NJ, USA: Wiley, Nov. 2013.

[12] M. Mabhula and M. J. Kamper, "Design optimization of cylindrical-rotor synchronous-induction motors," in *Proc. IEEE Energy Convers. Congr. Expo.*, 2018, pp. 5778–5785.

[13] X. Liang, S. O. Faried, and A. M. El-Serafi, "Space harmonics of synchronous machines calculated by finite-element method," *IEEE Trans. Ind. Appl.*, vol. 52, no. 2, pp. 1193–1203, Mar. 2016.

[14] N. Stranges, "Calculation of the starting performance of solid pole synchronous motors by the time-stepping finite element method," in *Proc. IEEE Power Energy Soc. General Meeting - Convers. Del. Elect. Energy 21st Century*, Jul. 2008, pp. 1–4, doi: 10.1109/PES.2008.4596486.

[15] B. Vaseghi, B. Nahid-mobarakh, N. Takorabet, and F. Meibody-Tabar, "Inductance identification and study of PM motor with winding turn short circuit fault," *IEEE Trans. Magn.*, vol. 47, no. 5, pp. 978–981, May 2011.

[16] J. Lammeraner and M. Štafl, *Eddy Currents.* London: Iliffe, 1966.